

# A new Lagrangian drift mechanism due to current–bathymetry interactions: applications in coastal cross-shelf transport

Akanksha Gupta<sup>1,2†</sup> and Anirban Guha<sup>2</sup>

<sup>1</sup>Department of Mechanical Engineering, Indian Institute of Technology, Kanpur, U.P. 208016, India.

<sup>2</sup>School of Science and Engineering, University of Dundee, DD1 4HN, U.K.

(Received xx; revised xx; accepted xx)

We show that in free surface flows, a uniform, streamwise current over small-amplitude rippled bottom topography generates cross-stream drift velocity. This Lagrangian drift, referred to as the current-bathymetry interaction induced drift (CBIID), is specifically understood in the context of a simplified nearshore environment, consisting of uniform alongshore current, onshore propagating surface waves, and monochromatic rippled bathymetry making an oblique angle with the shoreline. CBIID is found to originate from the steady, non-homogeneous solution of the governing system of equations. Similar to Stokes drift induced by surface waves, CBIID can also have important implications in cross-shelf tracer transport. CBIID increases with particle's depth, bottom ripple's wavelength and amplitude, and the magnitude of the alongshore current. Moreover, maximum cross-shelf transport by CBIID is obtained when the bottom ripple wave-vector approximately makes  $\pi/4$  angle with the shoreline. Depending on the angle between the alongshore current and the bottom ripple wave-vector, CBIID can lead to onshoreward or offshoreward tracer transport. Unlike Stokes drift, particle excursions due to current-bathymetry interactions might not be small, hence analytical expressions based on small-excursion approximation could be inaccurate. We provide an alternative  $z$ -bounded approximation, which provides highly accurate expressions of drift velocity and time period for particles near the free surface. Realistic parametric analysis reveals that in situations where the Stokes drift and CBIID velocities have comparable magnitudes, they are order separated both in length and time scales. We infer that high-resolution coastal bathymetry maps are crucial for accurate predictions of tracer transport pathways in the nearshore environment.

**Key words:**

## 1. Introduction

Rivers, estuaries, and coastal oceans are some examples of free surface flow environments that often exhibit shallow depths (few meters), moderately strong currents (up to

---

† Email address for correspondence: akanksha.gupta.iitbhu@gmail.com

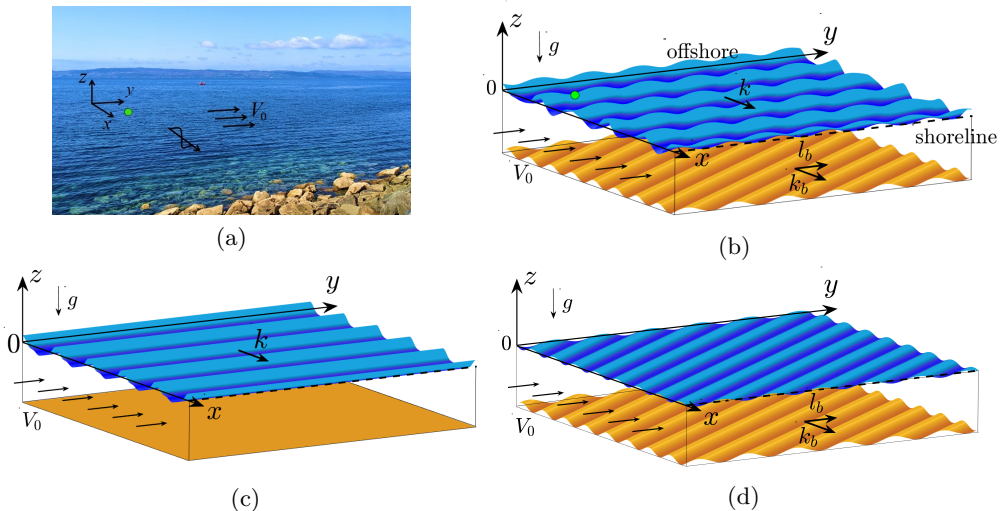


Figure 1: (a) A typical nearshore environment (location: Mallaig, Highlands of Scotland), and (b) the corresponding schematic diagram showing surface waves (wavenumber  $K(k, 0)$ ), alongshore current ( $V_0$ ), rippled bottom topography (wavenumber  $K_b(k_b, l_b)$ ) and the free surface imprint resulting from current–bathymetry interactions. Two subsets of the above situation are considered: (c) surface waves, flat bottom and alongshore current, and (d) rippled bottom topography and alongshore current, but no surface waves. In the last case, the undulations at the free surface represent the surface imprint of the rippled seabed. The black dashed line is used for the shoreline, and the green dot in (a, b) represents a particle at the ocean surface.

few meters per second), and fairly complex bottom topography. The free surface flow that we will particularly focus on is the nearshore environment – the transition region between the shoreline and the open ocean; see figure 1 (a). The nearshore region horizontally stretches for approximately 1 km, and consists of the surf zone (region of wave breaking) and the inner shelf (depths varying between a few meters to tens of meters) (Lentz & Fewings 2012; Kumar & Feddersen 2017). Cross-shelf transport, i.e. the exchange of sediments, pollutants, nutrients, larvae, and pathogens between the coastal waters and the open ocean, is arguably the central problem in coastal physical oceanography (Lentz *et al.* 2008; Brink 2016). Although cross-shelf currents are much weaker than alongshore currents, where the latter can often reach a velocity of 1–2 m/s in the surf zone (Oltman-Shay *et al.* 1989) and 0.1–0.8 m/s in the inner shelf region (Mukherjee 2014), cross-shelf gradients of most properties are usually far greater than those in the alongshore direction. This causes cross-shelf exchange to dominate the rates and pathways of tracer delivery and removal on the continental shelf (Brink 2016). Onshore propagating surface waves lead to cross-shelf transport in the onshore direction via the Stokes drift mechanism – net mass transport in the direction of surface wave propagation (Stokes 1847), while Eulerian return flow and transient rip currents are some of the important mechanisms causing offshore transport (Lentz *et al.* 2008; Brown *et al.* 2015; Kumar & Feddersen 2017; O’Dea *et al.* 2021).

The schematic in figure 1 (b) provides an idealized representation of figure 1 (a). This idealized scenario consists of three key elements: (i) a steady, uniform, alongshore current, (ii) onshore propagating monochromatic surface waves, and (iii) a small amplitude, monochromatic bottom topography with wave-vector making an oblique angle with the shoreline. According to our current understanding, the motion of a tracer parcel is expected to result from two different mechanisms: Stokes drift and longshore drift

(advection by the alongshore current). For the simplified set-up given in figure 1(b), a tracer parcel will move in a resultant direction whose streamwise component is along  $+y$  (due to the longshore drift) and cross-stream component is along  $+x$  (or onshore, due to the Stokes drift). The question we ask is – if we replace the set-up in figure 1(b) with a flat bathymetry (see figure 1(c)), does it alter the trajectory of a given tracer parcel? The primary objective of this paper is to show that small amplitude rippled topography *indeed* affects tracer trajectories, and in fact, can play a crucial role in cross-shelf tracer transport<sup>†</sup>.

The fact that small amplitude bottom topography can impact cross-shelf tracer transport is non-intuitive. If we assume surface waves in figure 1(a) or 1(b) to be absent, basic fluid mechanics tells us that the tracer parcel marked by green dot will be simply advected in the  $+y$  direction by the alongshore current (i.e. undergo longshore drift). In the presence of small amplitude topography, we will show that an additional mechanism is at play, which can lead to cross-shelf (along  $+x$  or  $-x$ ) tracer transport. The proposed mechanism owes its existence to the principles of open-channel hydraulics, according to which a steady, uniform current over a complex bathymetry yields a steady imprint of the bottom topography on the free surface (Henderson 1996; Chaudhry 2007). The steady surface imprints present in figure 1(b) can be unravelled by removing the surface waves entirely, see figure 1(d). The amplitude of these surface imprints may not be insignificant in fluvial and coastal environments owing to their shallow depths and high velocity scales, and hence can lead to non-trivial kinematics.

The outline of the paper is as follows. In §2, we provide the general mathematical formulation of the problem. In §3, we concentrate on figure 1(c) and onshore tracer transport of floating particles due to Stokes drift. §4 focuses on figure 1(d) and reveals a new Lagrangian drift mechanism resulting from the alongshore current and rippled seabed interactions. How this drift mechanism can contribute to the cross-shelf transport, and hence affect the fate of tracer parcels, is discussed in detail. In §5 we discuss the set-up in figure 1(b), i.e. the combined effect of surface waves, rippled seabed, and alongshore current. The paper is summarized and concluded in §6.

## 2. Mathematical formulation

We consider the three-dimensional (3D) problem of wave propagation over a rippled seabed in the presence of uniform background current; see figure 1(b). We assume the fluid to be irrotational, incompressible, inviscid, and homogeneous; the domain has infinite horizontal extent but has a finite depth  $H$ . Surface tension and Coriolis effects are neglected. The water surface is denoted by  $z = \eta(x, y, t)$ ;  $x$  and  $y$  respectively denote the cross-shelf (onshore and offshore are used respectively for positive and negative  $x$ -directions) and the alongshore directions, while the  $z$ -axis is directed upwards. The rippled seabed (or bottom surface) is denoted by  $z = -H + \eta_b(x, y)$ . We also consider a uniform cross-shelf current,  $U_0$ , and a uniform alongshore current,  $V_0$ . The fluid motion is defined by a velocity potential, which is a combination of the velocity potential due to the uniform currents, and the perturbed velocity potential ( $\phi$ ). The perturbed velocity potential satisfies the governing Laplace equation (GLE)

$$[\text{GLE}] : \quad \phi_{,xx} + \phi_{,yy} + \phi_{,zz} = 0, \quad (2.1)$$

where the comma subscript denotes partial derivative ( $\phi_{,x} = \partial\phi/\partial x$ ). Impenetrability

<sup>†</sup> For generic shallow, free surface flows with strong streamwise currents, this would imply cross-stream tracer transport.

condition (ImC) holds at the rippled seabed,  $z = -H + \eta_b(x, y)$ ,

$$[\text{ImC}] : \quad \phi_{,z} - \phi_{,x}\eta_{b,x} - \phi_{,y}\eta_{b,y} = U_0\eta_{b,x} + V_0\eta_{b,y}. \quad (2.2)$$

ImC is a non-homogeneous equation in general, and would lead to a homogeneous solution *only* when the level sets of  $\eta_b$  are parallel to the background current field. The kinematic (KBC) and dynamic boundary conditions (DBC) at the free water surface,  $z = \eta(x, y, t)$ , are respectively given as

$$[\text{KBC}] : \quad \eta_{,t} + (\phi_{,x} + U_0)\eta_{,x} + (\phi_{,y} + V_0)\eta_{,y} - \phi_{,z} = 0, \quad (2.3a)$$

$$[\text{DBC}] : \quad \phi_{,t} + \frac{1}{2}[(\phi_{,x})^2 + (\phi_{,y})^2 + (\phi_{,z})^2] + U_0\phi_{,x} + V_0\phi_{,y} + g\eta = 0, \quad (2.3b)$$

where  $g$  denotes gravitational acceleration. Hereafter, unless specifically mentioned, velocity or velocity potential will *always* imply perturbed quantities.

Next, the velocity potential at  $z = -H + \eta_b$  and  $z = \eta$  are respectively Taylor expanded about  $z = -H$  and  $z = 0$ . At the lowest order, we obtain the following linearized boundary conditions (BCs):

$$[\text{ImC}] : \quad \phi_{,z} = U_0\eta_{b,x} + V_0\eta_{b,y}, \quad \text{at } z = -H, \quad (2.4a)$$

$$[\text{KBC}] : \quad \eta_{,t} + U_0\eta_{,x} + V_0\eta_{,y} - \phi_{,z} = 0, \quad \text{at } z = 0, \quad (2.4b)$$

$$[\text{DBC}] : \quad \phi_{,t} + U_0\phi_{,x} + V_0\phi_{,y} + g\eta = 0, \quad \text{at } z = 0. \quad (2.4c)$$

Hereafter we assume  $U_0 \ll V_0$  (and further assume  $U_0 \approx 0$ ), since away from the inlets or river mouths, cross-shelf flows are typically much weaker than alongshore flows (Gelfenbaum 2005). We also consider two (small) spatial scales: wave steepness,  $\epsilon = Ka$  and rippled seabed steepness,  $\epsilon_b = K_b a_b$ , and expand the velocity potential ( $\phi$ ) and surface elevation ( $\eta$ ) as perturbation series in terms of  $\epsilon$  and  $\epsilon_b$ . Here,  $K$  is surface wave's wavenumber and  $a$  is its amplitude, while  $K_b$  is rippled seabed's wavenumber and  $a_b$  is its amplitude. The velocity potential and surface elevation can then be expressed in terms of  $\epsilon$  and  $\epsilon_b$  as

$$\phi = [\phi_u^{(1)} + O(\epsilon^2)] + [\phi_s^{(1)} + O(\epsilon_b^2)], \quad (2.5a)$$

$$\eta = [\eta_u^{(1)} + O(\epsilon^2)] + [\eta_s^{(1)} + O(\epsilon_b^2)]. \quad (2.5b)$$

Both  $\phi$  and  $\eta$  are a combination of an unsteady solution, denoted by subscript ' $u$ ', and a steady solution, denoted by subscript ' $s$ ' (Kirby 1988; Fan *et al.* 2021). The quantities  $\phi_u^{(1)}$  and  $\eta_u^{(1)}$  are  $O(\epsilon)$ , while  $\phi_s^{(1)}$  and  $\eta_s^{(1)}$  are  $O(\epsilon_b)$ . In (2.5a)–(2.5b), the relationship between  $\epsilon$  and  $\epsilon_b$  are not yet established, hence they are separated by squared brackets. In the following sections, we will investigate different situations depending on the relationship between  $\epsilon$  and  $\epsilon_b$ . Moreover, throughout the paper we consider a rippled seabed of the form

$$\eta_b = a_b \cos(k_b x + l_b y), \quad (2.6)$$

where  $k_b$  and  $l_b$  are respectively the wavenumbers in the  $x$ - and  $y$ -directions, and  $K_b$  (mentioned above) is  $\sqrt{k_b^2 + l_b^2}$ . Without any loss of generality, we have assumed  $k_b$  and  $l_b$  as positive quantities. Since  $V_0$  can be either positive or negative, we can span the entire range of angle,  $0$  to  $\pi$ , between the bottom ripple wave-vector,  $\mathbf{K}_b$ , and  $V_0$ .

The velocity field can be straightforwardly obtained from the velocity potential:  $\mathbf{u} \equiv (u, v, w) = (\phi_{,x}, \phi_{,y}, \phi_{,z})$ . Out of the three components, the  $u$  velocity plays the most crucial role in the cross-shelf transport of particles. Figure 2 shows contour plots of  $u$

at an arbitrary time in the  $x$ – $z$  plane for different situations depending on the relation between  $\epsilon$  and  $\epsilon_b$  (these situations have been schematically depicted in figures 1 *b*–*d*).

The primary focus of this paper is to obtain the trajectory  $(x(t), y(t), z(t))$  of a tracer particle, which can be obtained by solving the pathline equations:

$$\frac{dx}{dt} = u(x, y, z, t), \quad \frac{dy}{dt} = V_0 + v(x, y, z, t), \quad \frac{dz}{dt} = w(x, y, z, t). \quad (2.7)$$

Tracer trajectories for the different cases, whose overviews are given in figures 1 and 2, will be discussed in the following sections. Unless otherwise mentioned, all tracer trajectories will be studied for particles *at* the free surface.

### 3. Case-I: Wave steepness dominates over rippled seabed steepness

$$[O(\epsilon_b) \ll O(\epsilon)]$$

Here we consider the situation depicted in figure 1 (*c*) where the wave steepness ( $\epsilon$ ) is much greater than the rippled seabed steepness ( $\epsilon_b$ ); i.e.  $O(\epsilon_b) \ll O(\epsilon)$ . In this situation, the bottom surface is perceived to be (nearly) flat. To study the unsteady wave motion over a finite (and constant) depth fluid  $H$  and constant alongshore current  $V_0$ , we substitute the perturbation series of  $\phi$  and  $\eta$  from (2.5*a*)–(2.5*b*) into the GLE and BCs, given in (2.4*a*)–(2.4*c*). At  $O(\epsilon)$  we find:

$$[\text{GLE}] : \quad \phi_{u,xx}^{(1)} + \phi_{u,yy}^{(1)} + \phi_{u,zz}^{(1)} = 0 \quad -H < z < 0, \quad (3.1a)$$

$$[\text{ImC}] : \quad \phi_{u,z}^{(1)} = 0 \quad \text{at } z = -H, \quad (3.1b)$$

$$[\text{KBC}] : \quad \eta_{u,t}^{(1)} + V_0 \eta_{u,y}^{(1)} - \phi_{u,z}^{(1)} = 0 \quad \text{at } z = 0, \quad (3.1c)$$

$$[\text{DBC}] : \quad \phi_{u,t}^{(1)} + V_0 \phi_{u,y}^{(1)} + g \eta_u^{(1)} = 0 \quad \text{at } z = 0. \quad (3.1d)$$

We assume a linear, progressive surface wave of the form

$$\eta_u^{(1)} = a \cos(kx + ly - \omega t), \quad (3.2)$$

and solve (3.1*a*)–(3.1*d*), yielding

$$\phi_u^{(1)} = \frac{a\bar{\omega}}{K} \frac{\cosh K(z + H)}{\sinh(KH)} \sin(kx + ly - \omega t). \quad (3.3)$$

Here  $a$  is the amplitude and  $\omega$  is the frequency of the surface gravity wave with wavenumber  $K$ ,  $\omega = \bar{\omega} + V_0 l$  and  $\bar{\omega} (= \sqrt{gK \tanh(KH)})$  is its intrinsic frequency, and  $k$  and  $l$  are respectively the components of  $K$  in the  $x$ - and  $y$ -directions<sup>†</sup>. The solution (3.2)–(3.3) is generally known as the *homogeneous (unsteady) solution* of progressive surface gravity waves in the presence of a constant background current in a constant water depth. Related (but not the same) set-ups have been thoroughly studied in Dommermuth & Yue (1987); Kirby (1988); Raj & Guha (2019); Gupta & Guha (2021).

From (3.3), the velocity field at  $O(\epsilon)$  can be straightforwardly obtained:  $\mathbf{u}^{(1)} = \nabla \phi_u^{(1)}$ . Contours of the  $x$ -component of  $\mathbf{u}^{(1)}$  (i.e.  $u^{(1)}$ ) at an arbitrary time have been

<sup>†</sup> For simplicity, schematic figures 1 (*a*), 1 (*b*), or 1 (*c*) show surface wave-vector only along  $x$ .

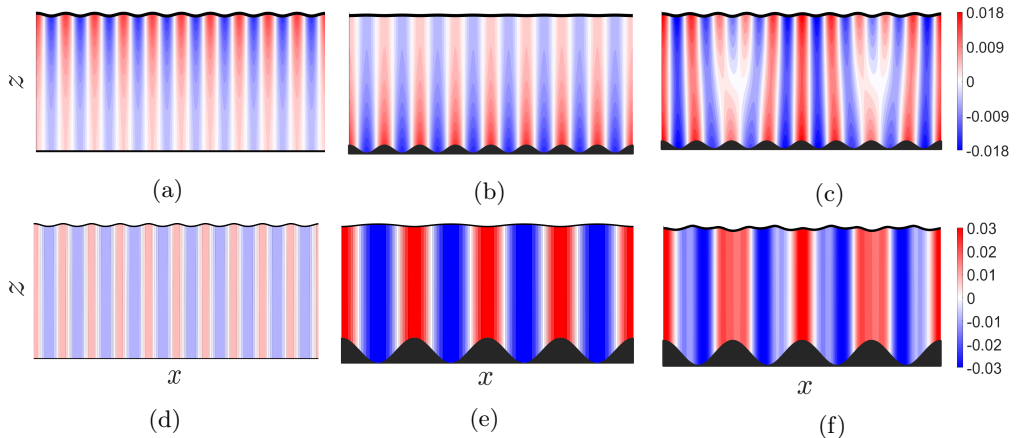


Figure 2: Contour plots of instantaneous cross-shelf velocity  $u$  in the  $x$ - $z$  plane for intermediate (a, b, and c) and shallow (d, e, and f) water depths. (a,d): case-I ( $O(\epsilon_b) \ll O(\epsilon)$ ), (b,e): case-II ( $O(\epsilon_b) \gg O(\epsilon)$ ), and (c,f): case-III ( $O(\epsilon_b) \sim O(\epsilon)$ ). Parameters used: (a)  $KH(kH, lH) = 2(2, 0)$ ,  $a/H = 0.01$ , (b)  $K_bH(k_bH, l_bH) = 2(1.6, 1.2)$ ,  $a_b/H = 0.03$ , (c) combined parameters of (a) and (b), (d)  $KH(kH, lH) = 0.2(0.2, 0)$ ,  $a/H = 0.01$ , (e)  $K_bH(k_bH, l_bH) = 0.1(0.08, 0.06)$ ,  $a_b/H = 0.1$ , and (f) combined parameters of (d) and (e).  $Fr \equiv |V_0|/\sqrt{gH} = 0.5$  in all cases.

respectively plotted in figures 2(a) and 2(d) for intermediate ( $KH \approx 1$ ) and shallow ( $KH \ll 1$ ) depths.

### 3.1. Pathline equations

Substitution of  $\mathbf{u}^{(1)}$  into (2.7) leads to the pathline equations for case-I:

$$\frac{dx}{dt} = \frac{a\bar{\omega}k}{K} \frac{\cosh K(z+H)}{\sinh(KH)} \cos \theta, \quad (3.4a)$$

$$\frac{dy}{dt} = V_0 + \frac{a\bar{\omega}l}{K} \frac{\cosh K(z+H)}{\sinh(KH)} \cos \theta, \quad (3.4b)$$

$$\frac{dz}{dt} = a\bar{\omega} \frac{\sinh K(z+H)}{\sinh(KH)} \sin \theta, \quad (3.4c)$$

where  $\theta = kx + ly - \omega t$ . Even for a linear water wave, a tracer particle moves in an open trajectory, which is obtained by solving the dynamical system (3.4a)–(3.4c) (Constantin & Villari 2008). Note that the alongshore current  $V_0$  Doppler shifts the frequency, but otherwise does not impact the cross-shelf transport. The forward drift in figure 3(a), which is the well-known *Stokes drift*, would lead to onshore particle transport.

### 3.2. Stokes drift: small-excursion approximation

The classical technique for calculating Stokes drift employs Taylor expansion by *a-priori* assuming that the particle excursion over one wave-period is small (Stokes 1847; Kundu *et al.* 2016; Van den Bremer & Breivik 2017). Equations (3.4a)–(3.4c) include a constant current  $V_0$ , hence for conducting small-excursion analysis about an initial particle location  $(x_0, y_0, z_0)$ , we first need to apply the following Galilean transformation:  $(X, Y, Z) = (x, y - V_0t, z)$  †. Closed trajectory is obtained at  $O(\epsilon)$ , but inclusion of  $O(\epsilon^2)$

† In a rest frame, there is always a displacement  $V_0t$  along  $y$  due to constant advection. This longshore drift may not be small, leading to a violation of the small-excursion approximation.

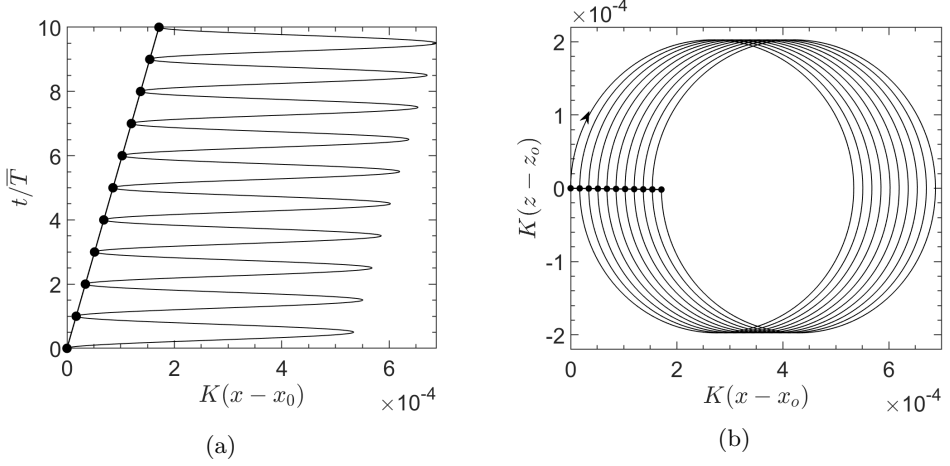


Figure 3: Particle trajectory for case-I in the non-dimensional (a)  $x$ - $t$  plane and (b)  $x$ - $z$  plane. These are plotted in a reference frame moving with alongshore current,  $V_0$ . The solid, wavy black line denotes the particle trajectory, while filled black circles are plotted after each  $\bar{T}$ . The black line connecting the circles is the Lagrangian mean trajectory of the particle. Parameters used:  $KH(kH, lH) = 1(1, 0)$ ,  $a/H = 0.01$ ,  $a_b/H = 0$ , and  $Fr = 0.1$  ( $V_0 > 0$ ).

terms reveal an open trajectory, shown in figure 3 (b), and yields the Stokes drift velocity:

$$\langle u_{SD} \rangle = \frac{a^2 \bar{\omega} k}{2 \sinh^2(KH)} \cosh[2K(z_0 + H)], \quad (3.5a)$$

$$\langle v_{SD} \rangle = \frac{a^2 \bar{\omega} l}{2 \sinh^2(KH)} \cosh[2K(z_0 + H)], \quad (3.5b)$$

$$\langle w_{SD} \rangle = 0, \quad (3.5c)$$

where  $\langle \dots \rangle$  denotes averaging over one wave period (in the moving frame),  $\bar{T} = 2\pi/\bar{\omega}$ . Equations analogous to (3.5a)–(3.5c) can be found in Ursell (1953); Gupta & Guha (2021). The small-excursion approximation, which serves the basis for (3.5a)–(3.5c), yields a highly accurate solution – for deep and shallow water waves, the errors are respectively  $O(\epsilon^6)$  (Longuet-Higgins 1987; Van den Bremer & Breivik 2017) and  $O(\epsilon^4)$  (Clamond 2007). The resulting Stokes drift displacement is

$$\Delta \mathbf{x}_{SD} = \langle \mathbf{u}_{SD} \rangle \bar{T},$$

and is the linear distance between two filled black circles shown in figure 3, where  $\bar{T} = T$  since  $l = 0$ . Among other things, we will scrutinize in the following sections whether *a-priori* assumption of small-excursion applied to the pathline equations yields highly accurate results when there is a rippled seabed and a background alongshore current.

#### 4. Case II: Rippled seabed steepness dominates over wave steepness [ $O(\epsilon_b) \gg O(\epsilon)$ ]

Here we consider the situation shown in figure 1 (d) – there is a uniform alongshore current ( $V_0$ ) over a rippled topography ( $\eta_b$ ), but surface waves are either absent or have negligible effects (mathematically,  $O(\epsilon_b) \gg O(\epsilon)$ ). To study this, we substitute

the perturbation series of  $\phi$  and  $\eta$  from (2.5a)–(2.5b) into the GLE and BCs, given in (2.4a)–(2.4c). At  $O(\epsilon_b)$ , we obtain the following set of steady, non-homogeneous system of equations:

$$[\text{GLE}] : \quad \phi_{s,xx}^{(1)} + \phi_{s,yy}^{(1)} + \phi_{s,zz}^{(1)} = 0 \quad -H < z < 0, \quad (4.1a)$$

$$[\text{ImC}] : \quad \phi_{s,z}^{(1)} = V_0 \eta_{b,y} \quad \text{at } z = -H, \quad (4.1b)$$

$$[\text{KBC}] : \quad V_0 \eta_{s,y}^{(1)} - \phi_{s,z}^{(1)} = 0 \quad \text{at } z = 0, \quad (4.1c)$$

$$[\text{DBC}] : \quad V_0 \phi_{s,y}^{(1)} + g \eta_s^{(1)} = 0 \quad \text{at } z = 0. \quad (4.1d)$$

The steady surface elevation and velocity potential, which results from the interaction between the rippled bottom boundary and the uniform alongshore current, and obtained by solving (4.1a)–(4.1d) along with (2.6), are respectively given by:

$$\eta_s^{(1)}(x, y, t) = a_s \cos(k_b x + l_b y), \quad \text{and} \quad (4.2a)$$

$$\phi_s^{(1)}(x, y, z, t) = \left[ A_s \frac{\cosh K_b(z + H)}{\cosh(K_b H)} + B_s \frac{\sinh(K_b z)}{\cosh(K_b H)} \right] \sin(k_b x + l_b y). \quad (4.2b)$$

Here,

$$\begin{aligned} a_s &= \frac{V_0^2 l_b^2 a_b}{[V_0^2 l_b^2 - g K_b \tanh(K_b H)] \cosh(K_b H)}, \\ A_s &= -\frac{V_0 l_b g a_b}{[V_0^2 l_b^2 - g K_b \tanh(K_b H)] \cosh(K_b H)}, \text{ and} \\ B_s &= -\frac{V_0 l_b a_b}{K_b}. \end{aligned}$$

The expressions (4.2a)–(4.2b) are the *particular (steady) solutions*, and result from the presence of the non-homogeneous term  $V_0 \eta_{b,y}$  in the R.H.S. of (4.1b). If either  $\eta_{b,y} = 0$  (i.e. no topographic variation in the alongshore direction) or  $V_0 = 0$ , there would be no steady surface impressions, and no steady velocity potential. We emphasize here that  $\eta_{b,y} = 0$  in (2.6) would imply  $a_b l_b = 0$ . Therefore, sinusoidal ripples ( $a_b \neq 0$  and  $k_b \neq 0$ ) with  $l_b = 0$  would still lead to a null or trivial particular solution. This is also evident from the dependence of  $a_s$ ,  $A_s$ , and  $B_s$  on  $l_b$ .

Figures 2(b) and 2(e) respectively show  $u^{(1)} (= \phi_{s,x}^{(1)})$ , where  $\phi_s^{(1)}$  is in (4.2b)) contours for intermediate and shallow depths. Figure 2(b) reveals an obvious, yet important fact that  $|u^{(1)}|$  is maximum at the bottom and decays with elevation, contrary to the behaviour observed in figure 2(a) (the intermediate depth situation for case-I, i.e. the ‘homogeneous’ problem). Additionally, figures 2(b) and 2(e) reveal a standard result of open-channel hydraulics – for sub-critical flow, i.e. when the Froude number,  $Fr \equiv |V_0|/\sqrt{gH} < 1$ , the surface impressions are  $\pi$  shifted from the bottom undulations.

#### 4.1. Pathline equations

Under the umbrella of the wide range of problems associated with the ‘water-wave theory’, probably the only known pathline equation is (3.4a)–(3.4c), or its minor variations (e.g. when background current is absent), yielding the celebrated Stokes drift, i.e. mass transport by surface waves. However, even when surface waves are absent, it is *still* possible to obtain pathline equations. In this case, the velocity field is obtained



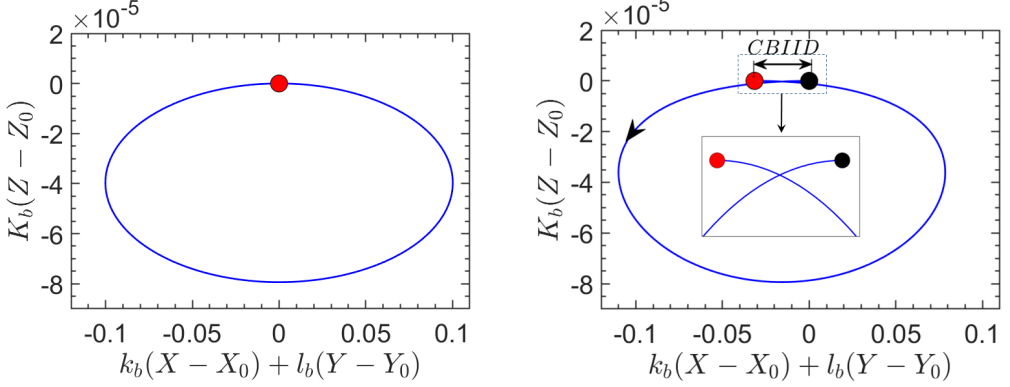


Figure 4: Particle trajectory in a reference frame moving with the alongshore current,  $V_0$ . Small-excursion approximation shows (a) closed trajectory at  $O(\epsilon_b)$ , and (b) open trajectory up to  $O(\epsilon_b^2)$ . The latter reveals CBIID, analogous to Stokes drift by surface waves. Filled black circle denotes initial position while filled red circle denotes position after one time period. Parameters used:  $a_b/H = 0.1$ ,  $K_b H(k_b H, l_b H) = 0.1(0.08, 0.06)$ ,  $a/H = 0$ ,  $Fr = 0.1$  ( $V_0 > 0$ ).

not from the homogeneous/unsteady solution *but* from the particular/steady solution  $\mathbf{u}^{(1)} = \nabla \phi_s^{(1)}$ . These pathline equations up to  $O(\epsilon_b)$  are given by:

$$\frac{dx}{dt} = k_b \left[ A_s \frac{\cosh K_b(z + H)}{\cosh(K_b H)} + B_s \frac{\sinh(K_b z)}{\cosh(K_b H)} \right] \cos \theta_b, \quad (4.3a)$$

$$\frac{dy}{dt} = V_0 + l_b \left[ A_s \frac{\cosh K_b(z + H)}{\cosh(K_b H)} + B_s \frac{\sinh(K_b z)}{\cosh(K_b H)} \right] \cos \theta_b, \quad (4.3b)$$

$$\frac{dz}{dt} = K_b \left[ A_s \frac{\sinh K_b(z + H)}{\cosh(K_b H)} + B_s \frac{\cosh(K_b z)}{\cosh(K_b H)} \right] \sin \theta_b, \quad (4.3c)$$

where  $\theta_b = k_b x + l_b y$ . As already mentioned,  $l_b \neq 0$  is necessary for the existence of a non-trivial particular solution. Furthermore, (4.3a) reveals that the pathline equation in the  $x$ -direction is dependent on  $k_b$ . Hence, both  $k_b \neq 0$  and  $l_b \neq 0$  are necessary for the existence of any motion in the  $x$  (i.e. cross-shelf) direction.

#### 4.1.1. Small-excursion approximation

We follow a procedure similar to what has been outlined in §3.2 – apply Galilean transform  $(X, Y, Z) = (x, y - V_0 t, z)$  to (4.3a)–(4.3c) and Taylor expand about an initial position, assuming that the excursion in one time period is small. Closed particle trajectory is obtained at  $O(\epsilon_b)$ , analogous to that obtained for surface waves at  $O(\epsilon)$ ; see figure 4(a). The locus is the equation of an ellipse:

$$\frac{(k_b X + l_b Y)^2}{(K_b^2 \mathcal{X}/V_0 l_b)^2} + \frac{(K_b Z)^2}{(K_b^2 \mathcal{Z}/V_0 l_b)^2} = 1, \quad (4.4)$$

where

$$\mathcal{X} = \left[ A_s \frac{\cosh K_b(z_0 + H)}{\cosh(K_b H)} + B_s \frac{\sinh(K_b z_0)}{\cosh(K_b H)} \right], \text{ and}$$

$$\mathcal{Z} = \left[ A_s \frac{\sinh K_b(z_0 + H)}{\cosh(K_b H)} + B_s \frac{\cosh(K_b z_0)}{\cosh(K_b H)} \right].$$

Hence, in the moving frame, particle trajectories are confined in a plane formed by

the bottom ripple wave-vector,  $\mathbf{K}_b$ , and the  $z$ -axis. Open trajectory shown in figure 4(b) is obtained at  $O(\epsilon_b^2)$ , analogous to that observed for surface waves at  $O(\epsilon^2)$ . We refer to this new kind of drift as the current-bathymetry interaction induced drift (CBIID). The *approximate*-CBIID (aCBIID) velocity, obtained using the small-excursion approximation (which is the analog of Stokes drift velocity (3.5a)–(3.5c) for surface waves), is given by

$$\langle \mathbf{u}_{aCBIID} \rangle = \langle (\mathbf{X} - \mathbf{X}_0) \cdot \nabla \mathbf{u}^{(1)} |_{\mathbf{X}=\mathbf{X}_0} \rangle, \quad (4.5)$$

where  $\mathbf{u}^{(1)}$  is evaluated in the moving frame. In component form, this finally yields

$$\langle u_{aCBIID} \rangle = -\frac{k_b K_b^2}{2V_0 l_b} (\mathcal{X}^2 + \mathcal{Z}^2), \quad (4.6a)$$

$$\langle v_{aCBIID} \rangle = -\frac{l_b K_b^2}{2V_0 l_b} (\mathcal{X}^2 + \mathcal{Z}^2), \quad (4.6b)$$

$$\langle w_{aCBIID} \rangle = 0, \quad (4.6c)$$

where  $\langle \dots \rangle$  denotes averaging over one time period in the moving frame,  $T_{aCBIID} = 2\pi/V_0 l_b$ .

Exact particle trajectories, obtained by solving (4.3a)–(4.3c), are plotted in figure 5 for different parameter regimes. These figures indeed show that the steady velocity field arising from the particular solution leads to a cross-shelf tracer transport. All configurations in figure 5 has  $V_0 > 0$ , leading to a CBIID displacement that is directed towards the offshore ( $x < 0$ ), as evident from (4.6a). Figures 5(a) and 5(b) show trajectories in the  $x$ – $t$  plane for the intermediate-depth or moderate-ripples limit ( $K_b H \approx 1$ ), while figures 5(c) and 5(d) show the same for the shallow-water or long-ripples limit ( $K_b H \ll 1$ ). For intermediate-depth and small bottom-ripple height (i.e.  $a_b/H \ll 1$ ), the trajectory obtained from the small-excursion approximation is nearly indistinguishable from that obtained from the exact solution; see figure 5(a). However, differences arise as the bottom-ripple height is increased to  $a_b/H = 0.1$ , see figure 5(b). For the shallow-water case, differences between the small-excursion approximation and the exact solution are visible even when bottom-ripple height is small (figure 5c), and the differences get larger with increasing the bottom-ripple height (figure 5d). We note in passing that figures 5(a) and 5(d) show  $t/T_{CBIID} \in [45, 50]$ ; during the initial times (not shown in figure), the small-excursion approximation is nearly indistinguishable from the exact solution. Moreover, for the deep-water or short-ripples case ( $K_b H \gg 1$ ), the small-excursion approximation matches nearly exactly with the exact solution even when  $a_b/H = 0.1$  (not shown in figure).

#### 4.1.2. Near-exact solution: the $z$ -bounded approximation

Since small-excursion approximation, in-spite of providing simple and useful expressions (4.6a)–(4.6c), does not provide highly accurate predictions for a portion of the parameter space, we devise an alternative approximation technique. Realizing that a

particle located at the free surface must satisfy  $-a_s \leq z \leq a_s$ , we assume  $z = z_0$  (where  $z_0$  is particle’s initial  $z$ -position at the free surface) in the eigenfunctions of (4.3a)–(4.3c):

$$\frac{dx}{dt} = k_b \underbrace{\left[ A_s \frac{\cosh K_b(z_0 + H)}{\cosh(K_b H)} + B_s \frac{\sinh(K_b z_0)}{\cosh(K_b H)} \right]}_{\mathcal{X}} \cos(k_b x + l_b y), \quad (4.7a)$$

$$\frac{dy}{dt} = V_0 + l_b \underbrace{\left[ A_s \frac{\cosh K_b(z_0 + H)}{\cosh(K_b H)} + B_s \frac{\sinh(K_b z_0)}{\cosh(K_b H)} \right]}_{\mathcal{X}} \cos(k_b x + l_b y), \quad (4.7b)$$

$$\frac{dz}{dt} = K_b \underbrace{\left[ A_s \frac{\sinh K_b(z_0 + H)}{\cosh(K_b H)} + B_s \frac{\cosh(K_b z_0)}{\cosh(K_b H)} \right]}_{\mathcal{Z}} \sin(k_b x + l_b y). \quad (4.7c)$$

We refer to these pathline equations as the ‘ $z$ -bounded approximation’. Note that the  $z$ -bounded approximation circumvents the need of small-excursion assumption, and hence Galilean transformation. Figure 5(a–d) reveal that the  $z$ -bounded approximation is highly accurate, and indistinguishable from the exact solution. This is also the case for the deep-water regime as well. Figure 5(e) shows the particle trajectory in the 3D space. The particle is always located on the free surface, and although is primarily advected along  $y$ , it does undergo a small drift along  $-x$ . The undulations on the free surface are the surface impressions of the rippled bottom.

#### 4.1.2.1. Time period and drift calculations

Like the small-excursion approximation, the  $z$ -bounded approximation has the advantage of providing a simple expression for the drift velocity, which is otherwise difficult to obtain from the exact equations (4.3a)–(4.3c). Equations (4.7a) and (4.7b) can be combined into a single equation

$$\frac{d\theta_b}{dt} = V_0 l_b + K_b^2 \mathcal{X} \cos \theta_b, \quad (4.8)$$

which is the key to finding the time period,  $T_{CBIID}$ :

$$T_{CBIID} = \frac{2\pi}{\sqrt{(V_0 l_b)^2 - (K_b^2 \mathcal{X})^2}} \approx T_{aCBIID} \left[ 1 + \frac{1}{2} \left( \frac{K_b^2 \mathcal{X}}{V_0 l_b} \right)^2 \right]. \quad (4.9)$$

Here,  $T_{CBIID}$  is the time taken by a particle to complete  $2\pi$  phase of its trajectory. In (4.9),  $K_b^2 \mathcal{X} \ll V_0 l_b$  (evident from (4.7b) and (4.8)), which reveals that  $T_{CBIID}$  is slightly longer than the time period  $T_{aCBIID} = 2\pi/V_0 l_b$  predicted from the small-excursion approximation. To calculate the CBIID velocity, we first divide (4.8) respectively with (4.7a), (4.7b), and (4.7c), and evaluate the CBIID displacement over one time period,  $T_{CBIID}$ , by integrating  $\theta_b$  from 0 to  $2\pi$ . CBIID velocity is obtained after dividing the CBIID displacement by  $T_{CBIID}$ :

$$\langle u_{CBIID} \rangle = -\frac{V_0 k_b l_b}{K_b^2} \left[ 1 - \sqrt{1 - (K_b^2 \mathcal{X}/V_0 l_b)^2} \right] \approx \langle u_{aCBIID} \rangle \frac{\mathcal{X}^2}{\mathcal{X}^2 + \mathcal{Z}^2}, \quad (4.10a)$$

$$\langle v_{CBIID} \rangle = -\frac{V_0 l_b^2}{K_b^2} \left[ 1 - \sqrt{1 - (K_b^2 \mathcal{X}/V_0 l_b)^2} \right] \approx \langle v_{aCBIID} \rangle \frac{\mathcal{X}^2}{\mathcal{X}^2 + \mathcal{Z}^2}, \quad (4.10b)$$

$$\langle w_{CBIID} \rangle = 0, \quad (4.10c)$$

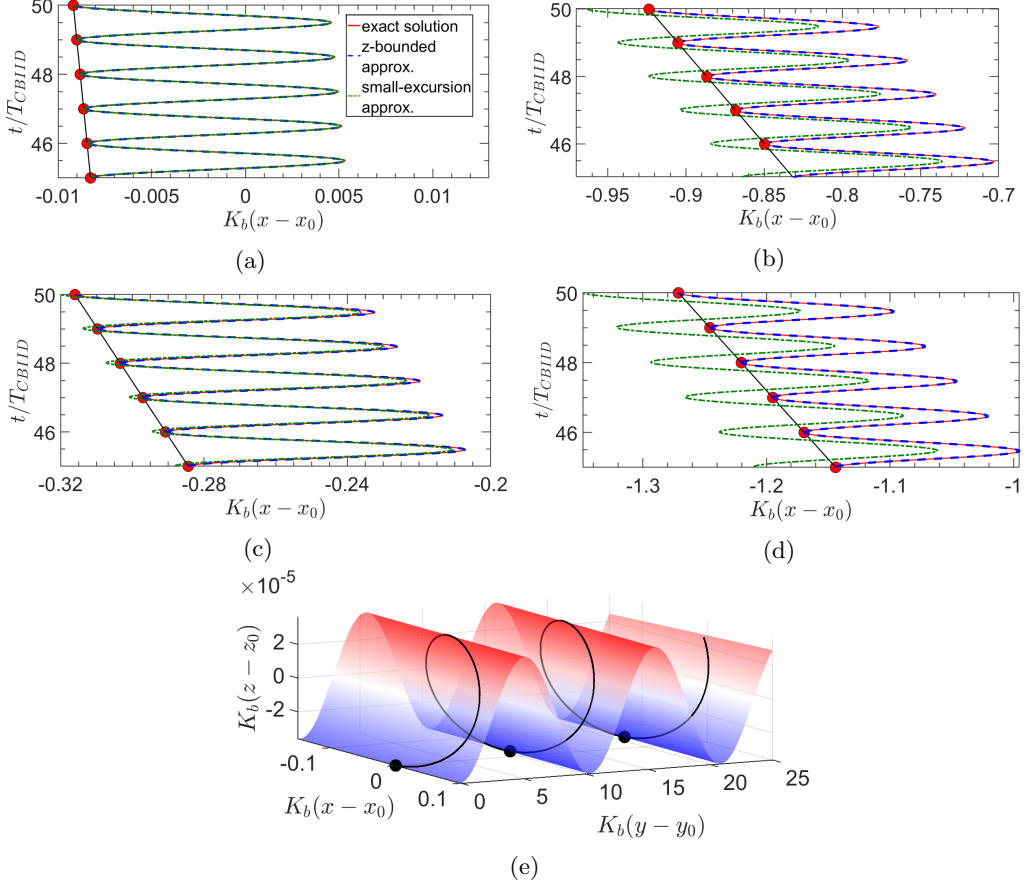


Figure 5: Particle trajectory for case-II, the non-homogeneous (steady) solution. Particle trajectory in the non-dimensional  $x-t$  plane for (a, b) intermediate-depth/moderate-ripples with  $K_b H(k_b H, l_b H) = 1(0.8, 0.6)$ , and (c, d) shallow-water/long-ripples with  $K_b H(k_b H, l_b H) = 0.1(0.08, 0.06)$ . Solid red, dashed blue, and dash-dotted green curves respectively denote the exact solution, the  $z$ -bounded approximation, and the small-excursion approximation. Filled red circles are plotted after each time period,  $T_{CBIID}$ , and are connected by the Lagrangian mean trajectory (solid black line). (e) Free surface impression,  $\eta_s$ , is shown by the surface plot for  $K_b H(k_b H, l_b H) = 0.1(0.08, 0.06)$ . Particle trajectory (which is always on the free surface) is shown by the solid black curve, and is plotted for the stationary reference frame. Filled black circles denote positions after each  $T_{CBIID}$ . Bottom ripple heights are as follows: (a)  $a_b/H = 0.01$ , (b)  $a_b/H = 0.1$ , (c)  $a_b/H = 0.05$ , and (d,e)  $a_b/H = 0.1$ . For all cases,  $a/H = 0$  (no surface wave) and  $Fr = 0.1$  ( $V_0 > 0$ ).

The above equations show that  $\langle \mathbf{u}_{CBIID} \rangle$  is not exactly the same as  $\langle \mathbf{u}_{aCBIID} \rangle$ , and hence provide another evidence for the disparity between the exact solution and the small-excursion approximation in figure 5 (a–d). Since shallow-water/long-ripples limit,  $k_b H \ll 1$  and  $l_b H \ll 1$ , and relatively high (but still a small quantity)  $a_b/H$  produces the maximum disparity (as shown in figure 5 d), the order of magnitude of this discrepancy needs to be evaluated. After a detailed but straight-forward algebra, we obtain

$$T_{CBIID}^{shallow} \approx T_{aCBIID} [1 + O((a_b/H)^2)], \text{ and } \langle \mathbf{u}_{CBIID}^{shallow} \rangle = \langle \mathbf{u}_{aCBIID} \rangle [1 + O(\epsilon_b^2)]. \quad (4.11)$$

Hence the relative difference between the two time periods scale with  $(a_b/H)^2$ , con-

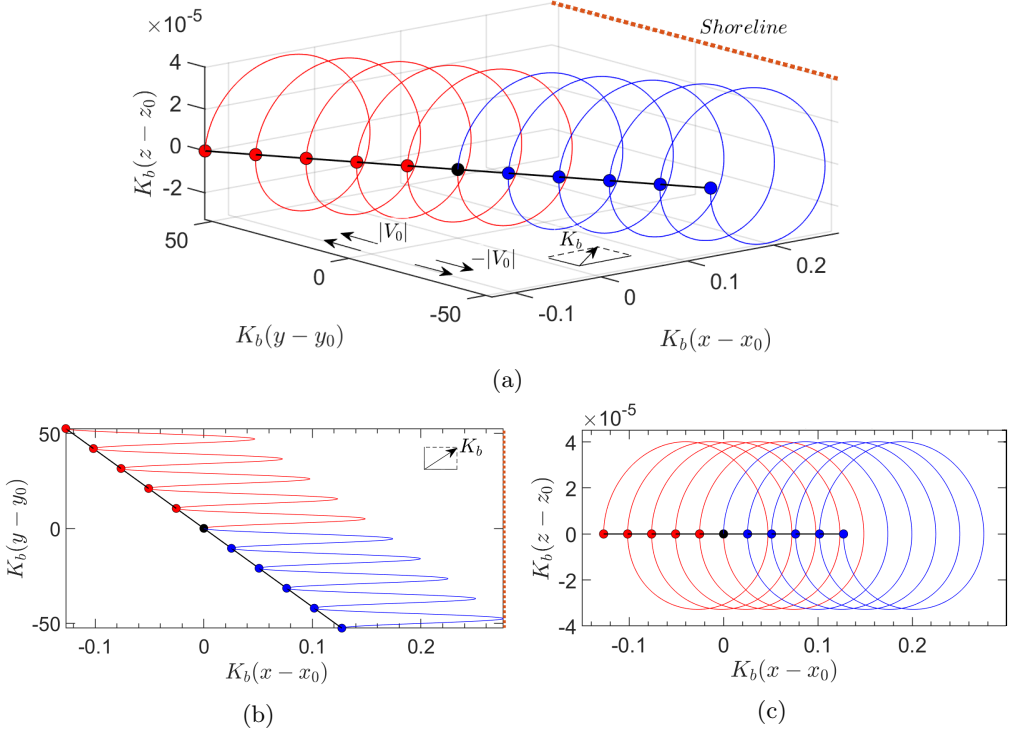


Figure 6: Particle trajectory for case-II in the stationary reference frame. Particle trajectory (a) in the 3D space, (b) in the  $x$ - $y$  plane, and (c) in the  $x$ - $z$  plane. Red (blue) solid line indicates trajectory when  $V_0 > 0$  ( $V_0 < 0$ ). The particle's initial position is shown by filled black circle, while red (blue) circle indicates particle's position after each time period ( $T_{CBIID}$ ) for  $V_0 > 0$  ( $V_0 < 0$ ). Parameters used:  $K_b H (k_b H, l_b H) = 0.1(0.08, 0.06)$ ,  $a_b/H = 0.1$ ,  $a/H = 0$ ,  $Fr = 0.1$ .

firming the discrepancies and the trend observed in figures 5(c) and 5(d). Since  $\epsilon_b = (k_b H)(a_b/H) \ll a_b/H$  (in the shallow-water limit), the error in evaluating  $\langle u_{aCBIID} \rangle$  is far less in comparison to that of  $T_{aCBIID}$ .

#### 4.2. Parametric analysis

##### 4.2.1. Effect of the alongshore current, $V_0$

Equation (4.10a) reveals that the magnitude of  $\langle u_{CBIID} \rangle$  is directly proportional to  $V_0$ , hence stronger alongshore current will produce stronger CBIID velocity in the cross-shelf direction. The sign of  $V_0$  determines whether the particles will travel onshore or offshore. When  $V_0 > 0$  ( $V_0 < 0$ ), CBIID displacement in the cross-shelf direction is negative (positive), i.e. particles will move towards the offshore (onshore direction). This is depicted in figure 6(a-c).

##### 4.2.2. Effect of the bottom ripple wave-vector, $\mathbf{K}_b$

Without loss of generality, we have limited the wave-vector angle,  $\beta \equiv \tan^{-1}(l_b/k_b)$  between 0 and  $\pi/2$ . However, since  $V_0$  can be either positive or negative, the angle between  $\mathbf{K}_b$  and the direction of  $V_0$  can range between 0 and  $\pi$ ; see figure 6(a).

Equation (4.10a),

$$\langle u_{CBIID} \rangle = -\frac{V_0}{2} \sin(2\beta) \left[ 1 - \sqrt{1 - (K_b^2 \mathcal{X} / V_0 l_b)^2} \right], \quad (4.12)$$

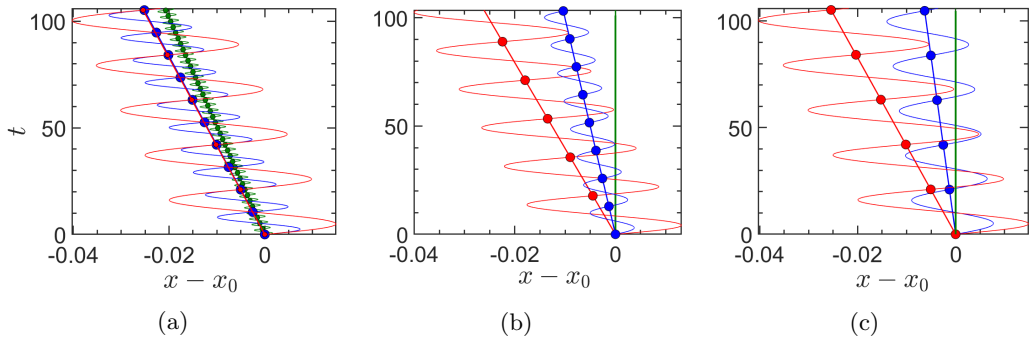


Figure 7: Particle trajectories for case-II;  $Fr = 0.1$  ( $V_0 > 0$ ) for all the sub-figures. (a) Different  $K_b H$  values for  $a_b = 0.1H$  and  $\beta = 0.205\pi$ :  $K_b H(k_b H, l_b H) = 0.1(0.08, 0.06)$  (red),  $K_b H(k_b H, l_b H) = 0.2(0.16, 0.12)$  (blue), and  $K_b H(k_b H, l_b H) = 0.8(0.64, 0.48)$  (green). (b) Different  $\beta$  values for  $a_b = 0.1H$  and  $K_b H = 0.1$ :  $\beta \approx \pi/4$  (red),  $\beta = 0.44\pi$  (blue), and  $\beta = \pi/2$  (green). (c) Different values of the bottom ripple's amplitude for  $K_b H = 0.1$  and  $\beta = 0.205\pi$ :  $a_b = 0.1H$  (red),  $a_b = 0.05H$  (blue), and  $a_b = 0$  (green).

re-written here for convenience, shows the dependence of the cross-shelf drift velocity on  $\beta$ . The magnitude of the wave-vector, i.e.  $K_b$ , can influence  $\langle u_{CBIID} \rangle$  via the term  $[\dots]$  in (4.12). This bracketed term, for shallow and deep water limits, are respectively as follows:

$$[\dots]_{shallow} \approx \frac{1}{2} \left( \frac{a_b/H}{Fr^2 \sin^2 \beta - 1} \right)^2,$$

$$[\dots]_{deep} \approx \frac{1}{2} (a_b K_b e^{-K_b H})^2.$$

Hence in the shallow-water limit, the magnitude of  $K_b$  does not affect the cross-shelf drift velocity. This behaviour is confirmed in figure 7(a), which is plotted for different  $K_b H$  values while keeping  $\beta$ ,  $a_b$ , and  $V_0$  fixed. It shows that for two different but small  $K_b H$  values,  $K_b H = 0.1$  (red), and  $0.2$  (blue), the Lagrangian mean trajectory (and hence  $\langle u_{CBIID} \rangle$ ) remains the same. We also observe that the time period of the red trajectory is twice of the blue trajectory. This stems from the fact that the time period is approximately  $2\pi/V_0 l_b$  (which is  $T_{aCBIID}$ ), and  $l_b H = 0.06$  for the red trajectory while  $l_b H = 0.12$  for the blue trajectory. Therefore, a particle following the red trajectory travels double the distance in one time period than that of the particle following the blue trajectory. Hence the filled red circles overlap with every alternate filled blue circles in figure 7(a). The deep water situation, however, shows a more complex dependence on  $K_b$ . It reveals that  $\langle u_{CBIID} \rangle$  decreases with an increase in  $K_b$ , which we have also confirmed numerically. We have plotted an intermediate depth situation,  $K_b H = 0.8$  (in green) in figure 7(a). Since  $l_b H = 0.48$  in this case, the time period is much lower than the shallow-water trajectories, and hence we find rapid oscillations in the green trajectory. We note that the maximum  $\langle u_{CBIID} \rangle$  is obtained in the shallow-water limit.

Figure 7(b) shows the effect of the wave-vector angle  $\beta$  on  $\langle u_{CBIID} \rangle$  while holding  $K_b$ ,  $a_b$ , and  $V_0$  fixed. Equation (4.12) reveals that  $\langle u_{CBIID} \rangle = 0$  when  $\beta = 0$  (i.e.  $l_b = 0$ ) or  $\pi/2$  (i.e.  $k_b = 0$ ), the latter is depicted by a green line in figure 7(b). The figure also shows the situation for which  $\langle u_{CBIID} \rangle$  is maximum (in red); for the parameters chosen, this occurs at  $\beta = \beta_{max} = 1.0054\pi/4$ , which was found numerically. For any other choice of  $\beta$ ,  $\langle u_{CBIID} \rangle$  is lower (in blue). We numerically found  $\beta_{max}$  close to  $\pi/4$  for different

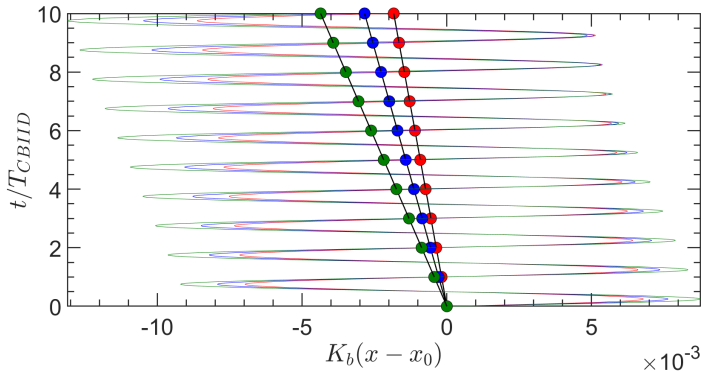


Figure 8: Particle trajectories for case-II; plotted for different initial  $z$  locations:  $z_0 = 0$  (red),  $z_0 = -H/2$  (blue) and  $z_0 = -3H/4$  (green). The solid curves show particle trajectory, while filled circles denote particle position after  $T_{CBIID}$  and connected by the Lagrangian mean trajectory (solid black line). Parameters used:  $K_b H(k_b H, l_b H) = 1(0.8, 0.6)$ ,  $a_b/H = 0.01$ ,  $Fr = 0.1$  ( $V_0 > 0$ ),  $a/H = 0$ .

choices of  $K_b$  and  $a_b$ ; this finding is not surprising given that the coefficient  $\sin(2\beta)$  in (4.12) attains the maximum value when  $\beta = \pi/4$ .

#### 4.2.3. Effect of the amplitude of the bottom ripple, $a_b$

Equation (4.6a) reveals that CBIID velocity in the cross-shelf direction is proportional to  $a_b^2$  (since  $\mathcal{X}^2$  and  $\mathcal{Z}^2$  are both proportional to  $a_b^2$ ), highlighting the crucial role played by bottom ripple’s amplitude in cross-shelf transport. The effect of  $a_b$  on particle trajectory, while holding all other parameters fixed, is shown in figure 7(c).

#### 4.2.4. Effect of particle’s initial $z$ -location, $z_0$

The fact that  $|u^{(1)}|$  is maximum at the bottom and decays with elevation, shown in figure 2(b), implies that CBIID will be higher for submerged particles (e.g. sediments) and lower for floating particles. This is evident in figure 8, which shows particle trajectories for three different initial  $z$  locations - at the surface (red), at the mid-depth (blue), and at three-quarters depth (green). These plots are obtained by exactly solving the pathline equations. Both small-excursion approximation and  $z$ -bounded approximation show differences with the exact solution, especially when  $z_0$  is near the bottom and  $a_b/H$  is relatively large (e.g.  $a_b/H \approx 0.1$ ). Since the  $z$ -bounded approximation assumes  $z$ -excursions to be small (hence approximates  $z$  with  $z_0$ ), this lead to non-negligible errors at greater depths where the  $z$ -excursion is larger.

### 5. Case-III: Wave steepness and rippled seabed steepness of the same order of magnitude [ $O(\epsilon_b) \sim O(\epsilon)$ ]

Here we consider a situation shown in figure 1(b) where the wave steepness ( $\epsilon$ ) is of the same order as rippled seabed steepness ( $\epsilon_b$ ); i.e.  $O(\epsilon_b) \sim O(\epsilon)$ . To study the linear interaction of the uniform alongshore current with the rippled bottom topography and surface waves, we substitute the perturbation series of  $\phi$  and  $\eta$  from (2.5a)–(2.5b) into

GLE and BCs, given in (2.4a)–(2.4c). At  $O(\epsilon)$  or  $O(\epsilon_b)$ , we obtain:

$$\phi_{,xx}^{(1)} + \phi_{,yy}^{(1)} + \phi_{,zz}^{(1)} = 0 \quad -H < z < 0, \quad (5.1a)$$

$$\phi_{,z}^{(1)} = V_0 \eta_{b,y} \quad \text{at } z = -H, \quad (5.1b)$$

$$\eta_{,t}^{(1)} + V_0 \eta_{,y}^{(1)} - \phi_{,z}^{(1)} = 0 \quad \text{at } z = 0, \quad (5.1c)$$

$$\phi_{,t}^{(1)} + V_0 \phi_{,y}^{(1)} + g\eta^{(1)} = 0 \quad \text{at } z = 0. \quad (5.1d)$$

Next, we assume the rippled bottom topography to be the same as that in case-II (given in (2.6)), and the surface wave profile to be the same as that considered in case-I (given in (3.2)). Hence the combined (i.e. unsteady + steady) solutions of the surface elevation and velocity potential are respectively as follows:

$$\eta^{(1)} = \eta_u^{(1)} + \eta_s^{(1)} = a \cos(kx + ly - \omega t) + a_s \cos(k_b x + l_b y), \quad (5.2a)$$

$$\begin{aligned} \phi^{(1)} = \phi_u^{(1)} + \phi_s^{(1)} = & \frac{a\bar{\omega}}{K} \frac{\cosh K(z+H)}{\sinh(KH)} \sin(kx + ly - \omega t) + \\ & \left[ A_s \frac{\cosh K_b(z+H)}{\cosh(K_b H)} + B_s \frac{\sinh(K_b z)}{\cosh(K_b H)} \right] \sin(k_b x + l_b y). \end{aligned} \quad (5.2b)$$

Figures 2(c) and 2(f) respectively show contour plots of cross-shelf velocity,  $u^{(1)} (= \phi_{,x}^{(1)})$ , where  $\phi^{(1)}$  is from (5.2b) for intermediate and shallow depths. While figure 2(a) reveals that  $|u^{(1)}|$  decreases with depth, and figure 2(b) shows exactly the reverse, their combination, figure 2(c), show a non-monotonic variation in  $|u^{(1)}|$  – surface waves dominating in the upper layer while current-bathymetry interactions dominating the bottom layer.

### 5.1. Pathline equations

The pathline equations can be obtained by substituting  $\mathbf{u}^{(1)} (= \nabla \phi^{(1)})$  into (2.7), which are as follows:

$$\begin{aligned} \frac{dx}{dt} = & \frac{a\bar{\omega}k}{K} \frac{\cosh K(z+H)}{\sinh(KH)} \cos(kx + ly - \omega t) + \\ & k_b \left[ A_s \frac{\cosh K_b(z+H)}{\cosh(K_b H)} + B_s \frac{\sinh(K_b z)}{\cosh(K_b H)} \right] \cos(k_b x + l_b y), \end{aligned} \quad (5.3a)$$

$$\begin{aligned} \frac{dy}{dt} = & V_0 + \frac{a\bar{\omega}l}{K} \frac{\cosh K(z+H)}{\sinh(KH)} \cos(kx + ly - \omega t) + \\ & l_b \left[ A_s \frac{\cosh K_b(z+H)}{\cosh(K_b H)} + B_s \frac{\sinh(K_b z)}{\cosh(K_b H)} \right] \cos(k_b x + l_b y), \end{aligned} \quad (5.3b)$$

$$\begin{aligned} \frac{dz}{dt} = & a\bar{\omega} \frac{\sinh K(z+H)}{\sinh(KH)} \sin(kx + ly - \omega t) + \\ & K_b \left[ A_s \frac{\sinh K_b(z+H)}{\cosh(K_b H)} + B_s \frac{\cosh(K_b z)}{\cosh(K_b H)} \right] \sin(k_b x + l_b y). \end{aligned} \quad (5.3c)$$

Figure 9(a) shows the trajectory plot obtained by solving the pathline equations (5.3a)–(5.3c). The figure reveals two spatial scales – one due to surface waves (fast oscillations) and the other due to CBIID (slow oscillations). To understand the reason behind the occurrence of two spatial scales, we perform a scatter plot of the two temporal scales,  $T$  and  $T_{CBIID}$ , in figure 9(b). We scanned a range of parameters (see caption of figure 9(b)) for which  $a/H \lesssim O(\epsilon)$  is satisfied, and we found  $T$  and  $T_{CBIID}$  to be order separated. While  $T$  is in the order of a few seconds (which is well known),  $T_{CBIID}$  is



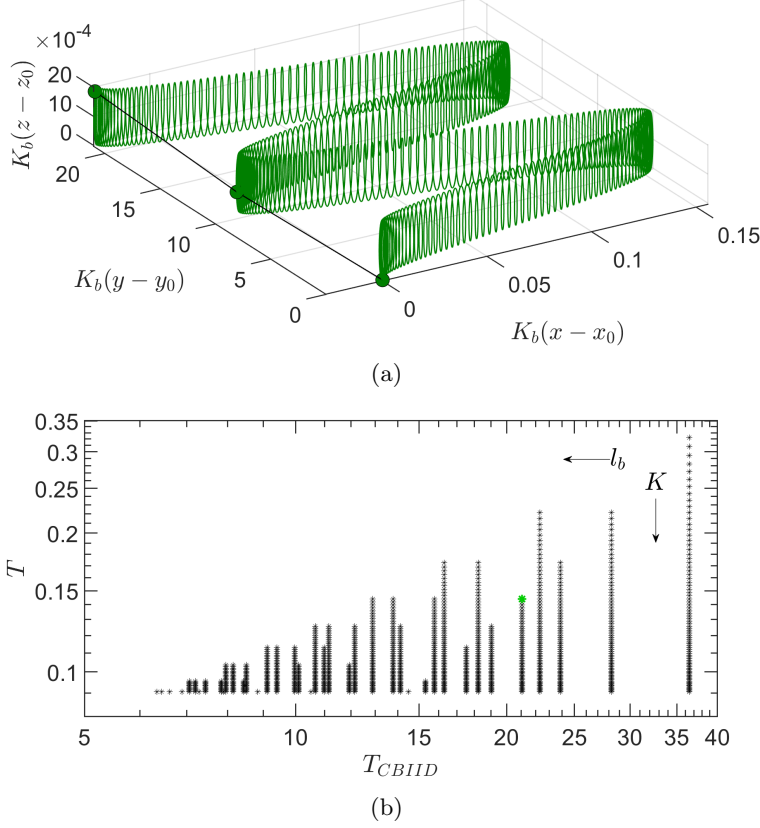


Figure 9: Case-III with  $a_b = 0.1H$  and  $Fr = 0.1$  ( $V_0 > 0$ ). (a) Particle trajectory in the non-dimensional 3D space, denoted by the solid green curve, is plotted for two time period(s). Filled green circles denote positions after each  $T_{CBIID}$ , and are connected by the Lagrangian mean trajectory. Here  $a = 0.01H$ , and  $KH(kH, lH) = 1(1, 0)$ ,  $K_bH(k_bH, l_bH) = 0.1(0.08, 0.06)$ . (b)  $T_{CBIID}$  v/s  $T$  plot for  $a \leq 0.01H$ , and the following range of wavenumbers:  $KH(kH, 0) = 0.2-2$ ,  $l_bH = 0.02-0.2$ . The green asterisk shows the case corresponding to sub-figure (a).

typically of the order of few minutes. The drift velocities,  $u_{SD}$  and  $u_{CBIID}$ , are found to have similar magnitudes, hence the spatial scale separation in figure 9(a) is exclusively due to the two time scales of the problem. To put the various ‘drift’ variables and their magnitudes into perspective, a comparison of case-I, -II, and -III for parameters deemed realistic in the nearshore environment is shown in table 1.

#### 5.1.1. Combined drift: small-excursion approximation

§4.1.1 has already revealed that small-excursion approximation might not provide highly accurate estimates, however in case-III, it is probably the only choice. While applying small-excursion approximation about an initial particle location  $\mathbf{X}_0 = (x_0, y_0, z_0)$ , we first need to implement Galilean transformation:  $(X, Y, Z) = (x, y - V_0t, z)$  to the pathline equation (5.3a)–(5.3c), and Taylor expand the pathline equations about the initial position. The particle motion depends on the combined effect of surface waves and current–bathymetry interaction; therefore, we refer to this drift as a combined drift (CD). The *approximate*-CD (aCD) velocity can be defined as,

---

	Non-dimensional			Dimensional		
	Cross-shelf displacement	Period	Drift velocity	Cross-shelf displacement (m)	Period (s)	Drift velocity (m/s)
Case-I	$1.69 \times 10^{-5}$	0.144	$1.17 \times 10^{-4}$	0.0042	5.094	$8.25 \times 10^{-4}$
Case-II	-0.0051	21.05	$-2.42 \times 10^{-4}$	-1.2711	744.34	$-1.71 \times 10^{-3}$
Case-III	-0.0026	21.05	$-1.23 \times 10^{-4}$	-0.5361	744.34	$-7.2 \times 10^{-4}$

---

Table 1: Cross-shelf displacement (in one period), corresponding time period, and drift velocity when  $Fr = 0.1$  ( $V_0 > 0$ ). Parameter used for case-I: surface wave-  $a/H = 0.01$ ,  $KH(kH, lH) = 1(1, 0)$ , case-II: bottom ripple-  $a_b/H = 0.1$ ,  $K_bH(k_bH, l_bH) = 0.1(0.08, 0.06)$ , and case-III: combination of case-I and -II. Parameters have been chosen such that  $\epsilon = \epsilon_b$ . For dimensional analysis, all variables are chosen accordingly for  $H = 5$  m. The drift in case-I, -II, and -III correspond to SD, CBIID, and SD+CBIID, respectively.

---

$$\langle u_{aCD} \rangle = \langle (\mathbf{X} - \mathbf{X}_0) \cdot \nabla \mathbf{u}^{(1)} |_{\mathbf{x}=\mathbf{x}_0} \rangle, \quad (5.4)$$

where

$$\begin{aligned} \mathbf{X} &= \mathbf{X}_u + \mathbf{X}_s, \\ \nabla \mathbf{u}^{(1)} &= \begin{bmatrix} u_{u,X}^{(1)} + u_{s,X}^{(1)} & v_{u,X}^{(1)} + v_{s,X}^{(1)} & w_{u,X}^{(1)} + w_{s,X}^{(1)} \\ u_{u,Y}^{(1)} + u_{s,Y}^{(1)} & v_{u,Y}^{(1)} + v_{s,Y}^{(1)} & w_{u,Y}^{(1)} + w_{s,Y}^{(1)} \\ u_{u,Z}^{(1)} + u_{s,Z}^{(1)} & v_{u,Z}^{(1)} + v_{s,Z}^{(1)} & w_{u,Z}^{(1)} + w_{s,Z}^{(1)} \end{bmatrix}, \end{aligned}$$

and  $\langle \dots \rangle$  denotes averaging over one time period,  $T_{aCD}$ , and each term of (5.4) is discussed in detail in appendix A.

While  $T_{aCD} = \text{LCM}(\bar{T}, T_{aCBIID})$  is the formal method for evaluation, its implementation is challenging in practice since  $\bar{T}$  and  $T_{aCBIID}$  are, in general, not integers (in fact, they are typically irrational numbers). The practical approach would be to approximate  $\bar{T}/T_{aCBIID}$  by its nearest rational number,  $n/m$  (i.e.  $m, n \in \mathbb{Z}^+$ ). This leads to  $T_{aCD} \approx nT_{aCBIID} \approx m\bar{T}$ , which is crucial for performing the averaging. Finally this yields (see appendix A)

$$\text{Lagrangian drift} \approx \text{Eulerian drift} + SD + CBIID.$$

## 5.2. Particle motion and comparison with the other two cases

Figure 10 provides a visual comparison of case-I, -II, and -III for the parameters given in table 1, in which  $\epsilon = \epsilon_b$ . Lagrangian mean trajectories reveal that case-I and -II result in oppositely directed cross-shelf transport, which has been discussed previously. The slope of these lines (which are inversely proportional to the corresponding drift velocities) have the same order of magnitude, which is evident from table 1 as well. The Lagrangian mean trajectory of case-III, being approximately the sum of cases-I and -II, turns out to be offshore directed for the chosen parameters. This finding has important implications in predicting the fate of tracers in the nearshore environment. If high resolution topographic variations in the nearshore region are not taken into

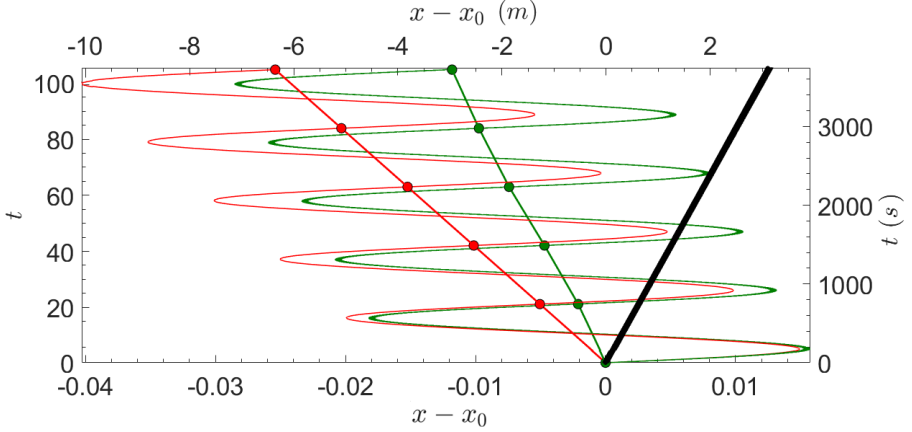


Figure 10: Particle trajectories in the dimensional (top and right axes) and non-dimensional (bottom and left axes)  $x$ - $t$  plane. Color scheme is as follows: case-I – black, case-II – red, and case-III – green. For each case, filled circles represent particle position after one time period, and the line joining these filled circles represent the Lagrangian mean trajectory. For parameters, see table 1 caption.

consideration, offshore tracer transport (green trajectory) might be mistakenly predicted as onshore transport (black trajectory).

Apart from the differences in Lagrangian mean motion, figure 10 also contrasts the excursions in case-I (which cannot be properly distinguished here, the zoomed-in version is shown in figure 3 *a*) with that in cases-II and -III. The excursions in the latter two cases are not very small, straight-forwardly implying that small-excursion approximation might not provide accurate results (a matter which we have discussed already). Due to the sizeable excursions in case-III (or case-II), a tracer parcel during initial times may be instantaneously at a location that is onshoreward in comparison to its initial position, while the mean trajectory is always directed towards the offshore. However after some time ( $t \gtrsim 5000$  s, not shown in figure), the instantaneous position of the particle, relative to its initial position, is always offshoreward.

## 6. Summary and conclusions

In this paper we have shown that in free surface flows, cross-stream drift velocity can be generated via the interactions between a uniform, streamwise current and small amplitude rippled bottom topography. This phenomenon is especially expected to have non-trivial implications in shallow free surface flows with strong currents. Focusing on a simple model of the nearshore environment, we hypothesize that the proposed Lagrangian drift mechanism (referred to as ‘CBIID’, which results from the alongshore current and rippled bathymetry interactions) can lead to the cross-shelf transport of nearshore tracers like planktons, pollutants, pathogens, and sediments. In coastal environments, cross-shelf tracer transport is often mediated through the Stokes drift mechanism – mass transport by surface waves. Mathematically, Stokes drift results from the transient, homogeneous part of the governing system of equations. Au contraire, the steady, non-homogeneous part of the governing equations give rise to CBIID. Depending on the angle between the alongshore current and the bottom ripple wave-vector, CBIID can lead to onshoreward or offshoreward tracer transport. The CBIID velocity in the cross-shelf direction,  $\langle \mathbf{u}_{CBIID} \rangle$ , is maximum when the bottom ripple wave-vector approximately makes an angle of

$\pi/4$  with the shoreline. Moreover,  $\langle \mathbf{u}_{CBIID} \rangle$  also increases with particle's initial depth (hence submerged particles will experience it more strongly than floating particles), the magnitudes of the alongshore current and bottom ripple's wavelength, and the amplitude of the bottom ripples.

We also investigated whether *a-priori* assumption of small-excursion approximation, which is essential for providing a highly accurate expression for Stokes drift, also provides highly accurate estimates of CBIID. We show that for moderate and long wavelength bottom ripples, particle excursions may not be small, hence small-excursion approximation does not provide accurate estimates. To circumvent this issue, we introduced the 'z-bounded approximation', which (like small-excursion approximation) provides simple expressions for the drift velocity and time period. It is found to be highly accurate and indistinguishable from the exact solution at (and near) the free surface. Since z-excursions increase with water depth, the z-bounded approximation, however, does not provide accurate estimates of CBIID in the vicinity of the bottom topography.

We have limited our study to a model nearshore environment consisting of uniform alongshore current, onshore propagating surface waves, and monochromatic rippled bathymetry making an oblique angle with the shoreline. Hence we have ignored many important nearshore processes, for example, Coriolis effects, boundary layers, wind forcing, wave breaking, and transient rip currents. Moreover, coastal bathymetry is far more complex than what has been considered in our analysis. The key advantage of our simplified analysis lies in underpinning the drift mechanism arising through current-bathymetry interactions, which might not be evident if various complex processes are taken into consideration. Moreover, the model environment considered in our study represents a fairly generic free surface flow scenario, and hence can be extended to other natural water bodies like rivers and estuaries. Realistic parametric analysis of the nearshore environment has revealed that in situations where the Stokes drift and CBIID velocities have comparable magnitudes, they are order separated both in length and time scales. In this scenario, the Lagrangian drift can be represented as the sum of Eulerian drift, Stokes drift, and CBIID. Furthermore, we show that if bottom ripples are not taken into consideration (i.e. CBIID is absent), offshore tracer transport might be mistakenly predicted as onshore transport. Hence, obtaining high resolution coastal bathymetry map is essential for accurate prediction of nearshore tracer transport. While bathymetry reconstruction is an ongoing challenge, recent efforts have provided bathymetry maps at 15 arc-seconds resolution (Tozer *et al.* 2019). In addition, the upcoming Surface Water and Ocean Topography (SWOT) satellite mission is expected to reconstruct bathymetry at unprecedented resolution.

## Acknowledgment

A. Gupta thanks Commonwealth Split-site Ph.D. scholarship for funding support.

## Declaration of interests

The authors report no conflict of interest.

## Appendix A. Evaluation of combined drift in case-III using the small-excursion approximation:

The *approximate*-CD velocities in the  $x$ -,  $y$ -, and  $z$ - directions are respectively derived from (5.4), which are as follows

$$\begin{aligned} \langle u_{aCD} \rangle &= \underbrace{\langle \tilde{X}_u u_{u,X}^{(1)} + \tilde{Y}_u u_{u,Y}^{(1)} + \tilde{Z}_u u_{u,Z}^{(1)} \rangle}_{\text{Term-1}} + \underbrace{\langle \tilde{X}_s u_{s,X}^{(1)} + \tilde{Y}_s u_{s,Y}^{(1)} + \tilde{Z}_s u_{s,Z}^{(1)} \rangle}_{\text{Term-2}} + \\ &\quad \underbrace{\langle \tilde{X}_u u_{s,X}^{(1)} + \tilde{Y}_u u_{s,Y}^{(1)} + \tilde{Z}_u u_{s,Z}^{(1)} \rangle}_{\text{Term-3}} + \underbrace{\langle \tilde{X}_s u_{u,X}^{(1)} + \tilde{Y}_s u_{u,Y}^{(1)} + \tilde{Z}_s u_{u,Z}^{(1)} \rangle}_{\text{Term-4}}, \end{aligned} \quad (\text{A } 1a)$$

$$\begin{aligned} \langle v_{aCD} \rangle &= \underbrace{\langle \tilde{X}_u v_{u,X}^{(1)} + \tilde{Y}_u v_{u,Y}^{(1)} + \tilde{Z}_u v_{u,Z}^{(1)} \rangle}_{\text{Term-5}} + \underbrace{\langle \tilde{X}_s v_{s,X}^{(1)} + \tilde{Y}_s v_{s,Y}^{(1)} + \tilde{Z}_s v_{s,Z}^{(1)} \rangle}_{\text{Term-6}} + \\ &\quad \underbrace{\langle \tilde{X}_u v_{s,X}^{(1)} + \tilde{Y}_u v_{s,Y}^{(1)} + \tilde{Z}_u v_{s,Z}^{(1)} \rangle}_{\text{Term-7}} + \underbrace{\langle \tilde{X}_s v_{u,X}^{(1)} + \tilde{Y}_s v_{u,Y}^{(1)} + \tilde{Z}_s v_{u,Z}^{(1)} \rangle}_{\text{Term-8}}, \end{aligned} \quad (\text{A } 1b)$$

$$\begin{aligned} \langle w_{aCD} \rangle &= \underbrace{\langle \tilde{X}_u w_{u,X}^{(1)} + \tilde{Y}_u w_{u,Y}^{(1)} + \tilde{Z}_u w_{u,Z}^{(1)} \rangle}_{\text{Term-9}} + \underbrace{\langle \tilde{X}_s w_{s,X}^{(1)} + \tilde{Y}_s w_{s,Y}^{(1)} + \tilde{Z}_s w_{s,Z}^{(1)} \rangle}_{\text{Term-10}} + \\ &\quad \underbrace{\langle \tilde{X}_u w_{s,X}^{(1)} + \tilde{Y}_u w_{s,Y}^{(1)} + \tilde{Z}_u w_{s,Z}^{(1)} \rangle}_{\text{Term-11}} + \underbrace{\langle \tilde{X}_s w_{u,X}^{(1)} + \tilde{Y}_s w_{u,Y}^{(1)} + \tilde{Z}_s w_{u,Z}^{(1)} \rangle}_{\text{Term-12}}. \end{aligned} \quad (\text{A } 1c)$$

where  $\langle \dots \rangle$  denotes averaging over one time period in the moving frame,  $T_{aCD}$ . We have defined  $T_{aCD}$  such that  $T_{aCD} \approx nT_{aCBIID} \approx m\bar{T}$ , where  $m, n \in \mathbb{Z}^+$ . The various terms appearing in (A 1a)–(A 1c) are as follows:

$$\text{Term-1} = u_{SD}, \quad \text{Term-5} = v_{SD}, \quad \text{Term-9} = w_{SD},$$

where  $u_{SD}$ ,  $v_{SD}$ , and  $w_{SD}$  are respectively given in (3.5a), (3.5b), and (3.5c). Likewise,

$$\text{Term-2} = u_{aCBIID}, \quad \text{Term-6} = v_{aCBIID}, \quad \text{Term-10} = w_{aCBIID},$$

where  $u_{aCBIID}$ ,  $v_{aCBIID}$ , and  $w_{aCBIID}$  are respectively given in (4.6a), (4.6b), and (4.6c). Additionally,

$$\begin{aligned} \text{Term-3} + \text{Term-4} &= \frac{a(k_b V_0 l_b - k\bar{\omega})}{K V_0 l_b \sinh(KH)} \{ (kk_b + ll_b) \mathcal{X} \cosh K(z_0 + H) + K K_b \mathcal{Z} \sinh K(z_0 + H) \} \mathcal{I}, \\ \text{Term-7} + \text{Term-8} &= \frac{a(l_b V_0 l_b - l\bar{\omega})}{K V_0 l_b \sinh(KH)} \{ (kk_b + ll_b) \mathcal{X} \cosh K(z_0 + H) + K K_b \mathcal{Z} \sinh K(z_0 + H) \} \mathcal{I}, \\ \text{Term-11} + \text{Term-12} &= \frac{a}{V_0 l_b \sinh(KH)} \left[ \{ \bar{\omega}(kk_b + ll_b) + V_0 l_b K K_b \} \mathcal{X} (\mathcal{P} - \mathcal{R}) \sinh K(z_0 + H) + \right. \\ &\quad \left. K K_b (\bar{\omega} + V_0 l_b) \mathcal{Z} (\mathcal{P} + \mathcal{R}) \cosh K(z_0 + H) \right], \end{aligned}$$

where,

$$\begin{aligned}\mathcal{I} &= \frac{\cos\{(k - k_b)x_0 + (l - l_b)y_0 - \pi(m + n)\} \sin\{\pi(m + n)\}}{2\pi(m + n)} + \\ &\quad \frac{\cos\{(k + k_b)x_0 + (l + l_b)y_0 - \pi(m - n)\} \sin\{\pi(m - n)\}}{2\pi(m - n)}, \\ \mathcal{P} &= \frac{\sin\{(k + k_b)x_0 + (l + l_b)y_0 - \pi(m - n)\} \sin\{\pi(m - n)\}}{2\pi(m - n)}, \\ \mathcal{R} &= \frac{\sin\{(k - k_b)x_0 + (l - l_b)y_0 - \pi(m + n)\} \sin\{\pi(m + n)\}}{2\pi(m + n)}.\end{aligned}$$

Since  $m, n \in \mathbb{Z}^+$ , we have  $\mathcal{I} = \mathcal{P} = \mathcal{R} = 0$ , leading to zero values for Terms -3, -4, -7, -8, -11, and -12. This finally yields

$$\mathbf{u}_{aCD} = \mathbf{u}_{SD} + \mathbf{u}_{aCBIID}. \quad (\text{A } 2)$$

## REFERENCES

- VAN DEN BREMER, T. S. & BREIVIK, Ø. 2017 Stokes drift. *Philos. Trans. R. Soc. A* **376** (2111), 20170104.
- BRINK, K. H. 2016 Cross-shelf exchange. *Annu. Rev. Mar. Sci.* **8**, 59–78.
- BROWN, J. A., MACMAHAN, J. H., RENIERS, A. J. & THORNTON, E. B. 2015 Field observations of surf zone–inner shelf exchange on a rip-channelled beach. *J. Phys. Oceanogr.* **45** (9), 2339–2355.
- CHAUDHRY, M. H. 2007 *Open-channel flow*. Springer Science & Business Media.
- CLAMOND, D. 2007 On the lagrangian description of steady surface gravity waves. *J. of Fluid Mech.* **589**, 433–454.
- CONSTANTIN, A. & VILLARI, G. 2008 Particle trajectories in linear water waves. *J. Math. Fluid Mech.* **10** (1), 1–18.
- DOMMERMUTH, D. G. & YUE, D. K. P. 1987 A high-order spectral method for the study of nonlinear gravity waves. *J. Fluid Mech.* **184**, 267–288.
- FAN, J., ZHENG, J., TAO, A. & LIU, Y. 2021 Upstream-propagating waves induced by steady current over a rippled bottom: theory and experimental observation. *J. Fluid Mech.* **910**.
- GELFENBAUM, G. 2005 Coastal currents. *Encyclopedia of Coastal Science*, Springer pp. 259–260.
- GUPTA, A. & GUHA, A. 2021 Modified Stokes drift due to resonant interactions between surface waves and corrugated sea floor with and without a mean current. *Phys. Rev. Fluid.* **6** (2), 024801.
- HENDERSON, F. M. 1996 Open channel flow. *Macmillan*.
- KIRBY, J. T. 1988 Current effects on resonant reflection of surface water waves by sand bars. *J. Fluid Mech.* **186**, 501–520.
- KUMAR, N. & FEDDERSEN, F. 2017 The effect of Stokes drift and transient rip currents on the inner shelf. Part I: No stratification. *J. Phys. Oceanogr.* **47** (1), 227–241.
- KUNDU, P. K., COHEN, I. M. & DOWLING, D. R. 2016 *Fluid Mechanics (Sixth Edition)*. Academic Press.
- LENTZ, S. J., FEWINGS, M., HOWD, P., FREDERICKS, J. & HATHAWAY, K. 2008 Observations and a model of undertow over the inner continental shelf. *J. Phys. Oceanogr.* **38** (11), 2341–2357.
- LENTZ, S. J. & FEWINGS, M. R. 2012 The wind-and wave-driven inner-shelf circulation. *Annu. Rev. Mar. Sci.* **4**, 317–343.
- LONGUET-HIGGINS, M. 1987 Lagrangian moments and mass transport in Stokes waves. *J. Fluid Mech.* **179**, 547–555.
- MUKHERJEE, A. *et al.* 2014 Observed seasonal and intraseasonal variability of the East India Coastal Current on the continental slope. *J. Earth Syst. Sci.* **123** (6), 1197–1232.
- O’DEA, A., KUMAR, N. & HALLER, M. C. 2021 Simulations of the surf zone eddy field and cross-shore exchange on a nonidealized bathymetry. *J. Geophys. Res. Oceans* **126** (5).

- OLTMAN-SHAY, J., HOWD, P. A. & BIRKEMEIER, W. A. 1989 Shear instabilities of the mean longshore current: 2. field observations. *J. Geophys. Res. Oceans* **94** (C12), 18031–18042.
- RAJ, R. & GUHA, A. 2019 On Bragg resonances and wave triad interactions in two-layered shear flows. *J. Fluid Mech.* **867**, 482–515.
- STOKES, G. G. 1847 On the theory of oscillatory waves. *Trans. Camb. Philos. Soc.* **8**, 441.
- TOZER, B., SANDWELL, D. T., SMITH, W.H.F., OLSON, C, BEALE, J. R. & WESSEL, P 2019 Global bathymetry and topography at 15 arc sec: SRTM15+. *Earth Space Sci.* **6** (10), 1847–1864.
- URSELL, F. 1953 The long-wave paradox in the theory of gravity waves. *Math. Proc. Camb. Philos. Soc* **49** (4), 685–694.